IEEE Open Journal of Industry Applications

Received 23 April 2020; revised 28 June 2020; accepted 1 July 2020. Date of publication 7 July 2020; date of current version 23 July 2020. The review of this article was arranged by Editor E. B. Agamloh.

Digital Object Identifier 10.1109/OJIA.2020.3007781

A Wide Air Gap Flux Switching Bearingless Motor With Odd and Even Pole Pair Numbers

THOMAS HOLENSTEIN[1] (Student Member, IEEE), MARCEL SCHUCK[2] (Member, IEEE), AND JOHANN W. KOLAR[2] (Fellow, IEEE)

[1] Levitronix GmbH, 8005 Zurich, Switzerland
[2] Power Electronic Systems Laboratory, Swiss Federal Institute of Technology (ETH) Zurich, 8092 Zurich, Switzerland

CORRESPONDING AUTHORS: MARCEL SCHUCK (e-mail: schuck@lem.ee.ethz.ch)

ABSTRACT This paper introduces a bearingless motor topology with a magnet-free rotor that provides a higher rotor torque density and wider magnetic air gap compared to previously published topologies. The stray flux is minimized by using a stator with only eight teeth in temple configuration that contain permanent magnets. The motor performance is analyzed based on experimental prototypes, that were designed using 3D FEM simulations, for even and odd rotor pole pair numbers of six and nine, respectively. Control schemes that compensate parasitic radial forces to achieve stable magnetic levitation of the rotors are presented. The implemented prototypes reached a rotational speed of 2000 rpm and a maximum torque of 8 Nm.

INDEX TERMS Flux switching, high torque, magnetic levitation, reluctance rotor, temple motor, wide air gap machine.

I. INTRODUCTION

Bearingless slice motors, featuring a magnetically levitated rotor and a stator with a magnetically integrated bearing function [1], are used in several commercial products [2]. Due to the magnetic suspension, the rotor can be hermetically sealed and isolated from the stator in a simple manner. The rotor can be operated in its own containment without any mechanical contact under a wide range of environmental conditions. This is beneficial for applications such as ultra-pure, low-shear fluid handling, processing of aggressive chemicals, abrasive media, operation under extreme ambient temperatures, or single-use applications [3]–[5]. The use of a bearingless slice motor as a pump, blower, or mixer for such applications was initially proposed in [6].

Topologies of bearingless motors without permanent magnets (PMs) in the rotor have been published previously [7]. Such topologies can be designed to feature low mechanical complexity [8], a large air gap [9], or high torque per stator PM mass [10]. Reluctance rotors can provide advantages for operation at high temperatures at which PMs would demagnetize, for high speeds due to the higher material strength, and for disposable applications due to lower material costs of the rotor. However, the achievable torque is significantly lower than that of a comparable rotor PM topology [11]–[14], and a larger rotor (higher circumferential speeds, increased manufacturing cost) would be required to achieve the same torque for the same magnetic air gap length. Alternatively, the magnetic air gap length can be reduced, resulting in a worse thermal insulation of the rotor.

To overcome these limitations, a new bearingless temple motor topology [15], [16], as shown in Fig. 1, is presented in this work. Based on the targeted mixing application, the design is optimized to provide maximum performance per rotor volume, while the outer dimensions of the motor are uncritical. The stator is arranged around and below the rotor in the axial direction. This provides room for large windings that are required to achieve a high air gap flux density and torque. Unlike the conventional temple motor design [15], in which the stator and rotor consist of iron and PM material, respectively, the presented design features stator teeth that contain PMs. These PMs are tangentially magnetized in alternating directions (shown by red arrows in Fig. 1), resulting in a flux-switching characteristic. Most research on flux-switching permanent magnet (FSPM) motors has been carried out for small air gaps and large numbers of stator and rotor teeth, with 12/10 being a popular combination [17]–[19] with the lowest number of teeth. In this work, a low number of eight stator teeth in combination with an even number of six rotor

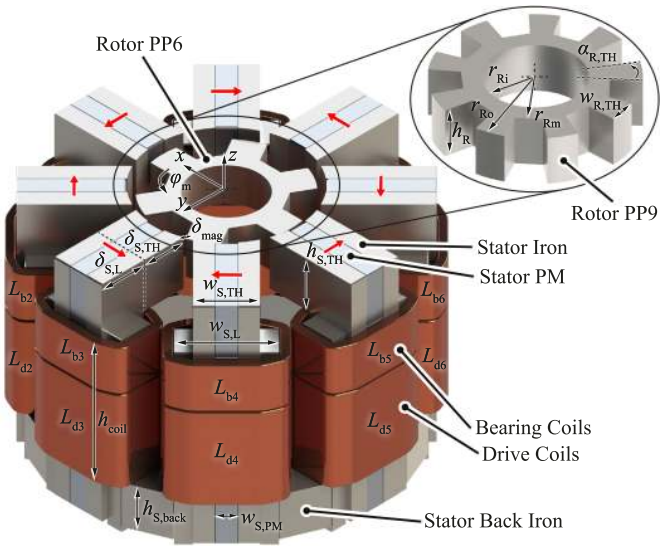

FIGURE 1. Rendering of the introduced bearingless eight-slot FSPM slice motor in temple configuration with separated drive and bearing windings. Two rotors with six and nine pole pairs were designed and compared to each other regarding the achievable motor performance. An explanation of the shown geometrical parameters is provided in Table 1.

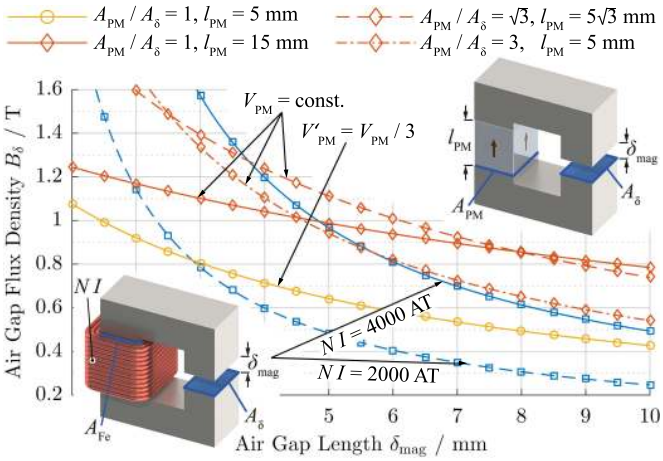

FIGURE 2. Flux density versus air gap length for ideal iron circuits without stray flux. The magnetic field is either generated by an energized coil or a PM. It can be seen that the dimensions of the PM significantly affect the scaling behavior of the magnetic flux density in the air gap.

teeth (FSPM PP6) as well as an odd number of nine rotor teeth (FSPM PP9) is explored. The resulting, comparably large structural sizes reduce the stray flux and enable a large ratio of the air gap to rotor radius, at the cost of a nonlinear, angle-dependent bearing force generation. Initial design considerations for the presented machine were outlined in [20].

Due to space constraints, and to avoid repetition of previously published materials, the basic principle of bearingless slice motors, including their characteristic equations regarding passive (mechanical stiffnesses) and active force and torque generation, are intentionally not repeated here. Detailed descriptions are available in the literature and can be found, e.g., in [6], [21]–[25].

The remainder of this paper is organized as follows: Section II provides considerations for the wide air gap design of magnetic circuits and Section III outlines the topology, operating principle, design procedure, and obtained characteristics of the introduced FSPM temple motor topology. In Section IV, a prototype implementation of the machine and measurement results are presented. Finally, Section V concludes the paper.

II. MOTOR DESIGN FOR WIDE AIR GAP

This section presents the underlying considerations for designing a motor topology that achieves high drive torque and passive stiffnesses while featuring a wide magnetic air gap. In the considered bearingless motor, radial forces, axial forces, tilting torques, and the motor torque are generated by magnetic attraction forces between the stator and the rotor. For an idealized iron circuit, the magnetic force

$$F_{\mathrm{mag}} = \frac{1}{2}\frac{B_\delta^2 \cdot A_\delta}{\mu_0} \tag{1}$$

between a stator pole and a rotor pole is proportional to the surface area of the pole faces A_δ as well as the flux density in the air gap B_δ and is $\approx 40\mathrm{N/cm}^2$ at $B_\delta = 1\mathrm{T}$ [26]. If the pole faces are shifted with respect to one another, the resulting force vector is directed along the magnetic flux lines and can be separated into a radial $F_{\mathrm{rad},i}$, tangential $F_{\mathrm{tan},i}$, and axial $F_{\mathrm{z},i}$ component for each stator tooth referenced by the index i. A radial force is generated if the tangential components of two opposing poles are pointing in the same direction. Otherwise, a drive torque is generated. Similarly, the axial components of two opposing poles either generate an axial force or a tilting torque, while a radial component can only result in radial forces.

A. TOPOLOGIES FOR FLUX GENERATION

The magnetic flux density in the air gap can be generated by a current flowing through an excitation coil or by a PM, as shown in Fig. 2. If stray fields are neglected, the flux densities can be calculated as

$$B_{\delta,\mathrm{coil}} = \frac{NI \cdot \mu_0}{\delta_{\mathrm{mag}} + \frac{l_{\mathrm{Fe}}}{\mu_{\mathrm{r,Fe}}}\frac{A_\delta}{A_{\mathrm{Fe}}}} \approx \frac{NI \cdot \mu_0}{\delta_{\mathrm{mag}}} \tag{2}$$

and

$$B_{\delta,\mathrm{PM}} = \frac{B_{\mathrm{R}}}{\frac{A_\delta}{A_{\mathrm{PM}}} + \frac{\delta_{\mathrm{mag}} \cdot \mu_{\mathrm{r,PM}}}{l_{\mathrm{PM}}} + \frac{\mu_{\mathrm{r,PM}}}{l_{\mathrm{PM}}}\frac{l_{\mathrm{Fe}}}{\mu_{\mathrm{r,Fe}}}\frac{A_\delta}{A_{\mathrm{Fe}}}} \approx \frac{B_{\mathrm{R}}}{\frac{A_\delta}{A_{\mathrm{PM}}} + \frac{\delta_{\mathrm{mag}}}{l_{\mathrm{PM}}}} \tag{3}$$

for the case of a coil and a PM, respectively. If the reluctance of the iron is neglected ($\mu_{\mathrm{r,Fe}} \to \infty$), $B_{\delta,\mathrm{coil}}$ only depends on the coil current I, the number of turns N, and the air gap length δ_{mag}, as outlined by the approximative expression in (2). From (2), it can be derived that a magnetic flux $\Theta = NI$ of $\approx 800\mathrm{AT}$ per one millimeter of δ_{mag} is required to achieve a flux density of $B_{\delta,\mathrm{coil}} = 1\mathrm{T}$ in the air gap.

If additionally $\mu_{\mathrm{r,PM}} = 1$ ($\mu_{\mathrm{r,NdFeB}} \approx 1.06$) is assumed, $B_{\delta,\mathrm{PM}}$ can be obtained based on the remanence flux density

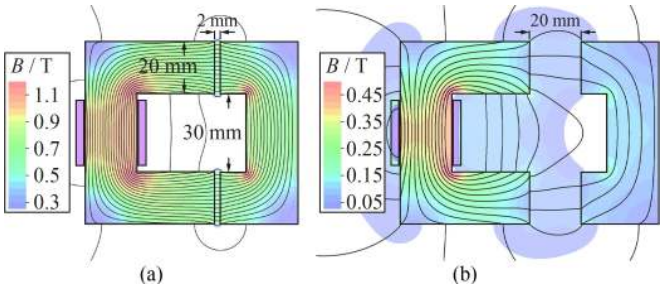

FIGURE 3. Stray flux for different structural sizes: 2D FEM simulation of an iron circuit at $\Theta = 2000$ AT with a small (a) and large (b) air gap with respect to the tooth width.

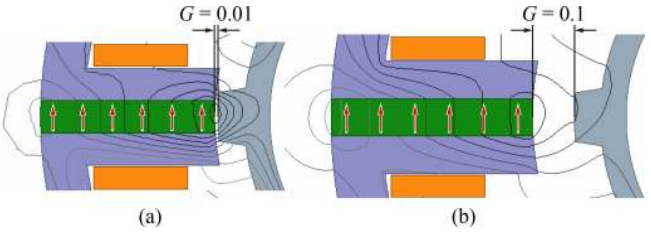

FIGURE 4. 2D FEM simulation of an FSPM topology with twelve stator teeth and ten rotor teeth with a small (a) and a large (b) air gap ratio *G*.

B_R of the PM and the ratios of the surface areas and thickness of the PM and the air gap, as outlined by the approximative expression in (3). In order to achieve $B_{\delta,PM} = B_R/2$, $A_{PM} = A_\delta$ and $l_{PM} = \delta_{mag}$ have to hold. To increase the flux density in the air gap, a significantly larger PM is required. To achieve $B_{\delta,PM} = 1$T with a N45 grade NdFeB PM ($B_R \approx 1.35$T), either l_{PM} or A_{PM} have to be tripled, or both dimensions have to be increased by 50 %, according to (3).

A coil and PMs can be combined to increase the magnetic field, as long as the iron is not saturated and the PM is not demagnetized, where the latter is usually uncritical for large air gaps.

B. AIR GAP SCALING

Based on (2) and (3), the effect of δ_{mag} on the magnetic flux density and, consequently, the forces and torques in the motor can be assessed. For this purpose, an iron circuit with a coil at two different excitations and iron circuits with four different PM geometries have been considered. The cross-sectional area of the magnetic air gap A_δ is identical for all cases. The resulting values of B_δ depending on the air gap length are shown in Fig. 2. The blue lines show the characteristics for the iron circuit with a coil that is excited with different flux values. The red lines show iron circuits with constant PM volumes, while the yellow line shows the case with one-third of the original PM volume. For all arrangements with PMs, the cross-sectional area of the leg of the back iron in which the PM is placed was chosen to be equal to A_{PM}. It can be observed that while $B_{\delta,coil}$ is approximately $\propto 1/\delta_{mag}$, a $B_{\delta,PM}$ that is significantly less sensitive to δ_{mag} can be obtained by using thick PMs.

However, the presented results have been obtained for neglected stray fields, which is only valid for small air gaps, as illustrated in Fig. 3. This is especially relevant for the considered slice motor topology as additional stray flux occurs above and below the motor, due to the flat design. As a result, the actual value of B_δ can be significantly lower than obtained by the simplified analytical calculations. To obtain the correct magnitude of the magnetic flux density, the space around the iron circuit has to be considered in addition, rendering analytical calculations infeasible, especially for complex geometries. For this reason, magnetic fields, forces, and torques are obtained by 3D FEM simulations in this work.

C. STRUCTURAL SIZES

Figure 4(a) and (b) show the flux lines for different ratios of the air gap to rotor radius $G = \delta_{mag}/r_{Ro}$ in the vicinity of a tooth for an exemplary flux switching motor topology with 12 stator teeth and 10 rotor teeth (12/10 motor configuration). It can be seen that the stray flux increases for an increasing value of G. Identical conditions are obtained if the number of stator and rotor teeth is halved (six stator teeth and five rotor teeth), while doubling the value of G at the same time. This shows that the stray flux is not determined by the absolute air gap length, but rather by its relative size compared to the other dimensions of the machine, such as the width and height of the stator and rotor poles. The shown results are identical to those obtained for the 8/6 and 8/9 configurations considered in this work, if G is increased according to the structural sizes. Consequently, a topology with a low number of stator teeth and rotor poles (big structural sizes of the motor components) should be chosen to maximize the air gap length. Dividing the stator teeth into multiple poles, as commonly implemented in conventional stepper motors and Vernier motors [27], [28] is disadvantageous in this case.

Contrary to the aforementioned effect, the achievable motor torque increases for a higher number of stator poles and teeth. For a given value of G, the motor torque will initially increase proportionally to the number of teeth and poles and subsequently decrease due to increased stray flux (small structural sizes). The ideal number of teeth and poles that results in the maximum torque decreases for increasing values of G.

D. PLACEMENT OF PERMANENT MAGNETS AND COILS

To achieve a maximum flux density within the air gap for large values of G, the coil or PM cannot be placed arbitrarily within the iron circuit. In order to prevent the flux lines from closing before passing through the air gap, the coil or PM should be placed as close to the air gap as possible. The resulting distributions of the magnetic field are shown in Fig. 5(a) and (b) for one big PM placed in the magnetic circuit far away from the air gap and two identical small PMs (combined volume equivalent to that of single big PM) placed directly next to the air gap, respectively. It can be observed that the flux density

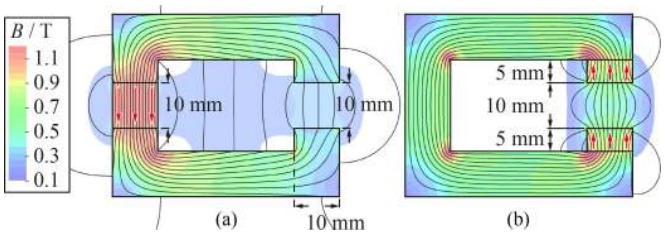

FIGURE 5. Field lines and flux density for identical PM (NdFeB N45) volume but different locations of the PMs in iron circuits with a large air gap relative to the tooth width. PMs placed far away from the air gap result in high stray flux (a) while low stray flux is obtained for placement close to the air gap (b).

within the air gap is higher in Fig. 5(b), despite a lower flux density within the magnets.

III. BEARINGLESS FSPM TEMPLE MOTOR

A. TOPOLOGY

The introduced FSPM topology features eight stator teeth that are divided up into tangentially sheeted electrical steel with a PM glued to their center. The PMs are magnetized tangentially in alternating directions, as shown by the red arrows in Fig. 1. This arrangement generates a heteropolar magnetic field in the air gap. Two concentrated coils are wound around each stator tooth, where the upper coil is used to generate radial forces (bearing coil) and the lower coil is used for torque generation (drive coil). To prevent saturation, the width of the stator teeth is increased in the area of the windings. The stator teeth are magnetically connected by individual back iron pieces made from axially sheeted electrical steel at the lower end of the motor. Two rotors were optimized for this stator, one with six (FSPM PP6) and one with nine rotor teeth (FSPM PP9) as displayed in Fig. 1. The rotor with six teeth results in a higher nominal torque, while the rotor with nine teeth provides advantages with regard to bearing force generation. The rotors are manufactured from axially sheeted electrical steel.

B. OPERATING PRINCIPLE

A characteristic property of bearingless slice motors is that only two radial degrees of freedom (DOF) need to be actively stabilized apart from rotation. Tilting in two DOF as well as axial displacements are passively stabilized by reluctance forces. Nevertheless, an applied force will lead to a deflection in the passive DOF and might excite weakly-damped oscillations. Therefore, rotor loads need to be carefully designed in terms of maximum load, center of gravity, and imbalance. Due to the sinusoidal back-EMF, the presented FSPM motor is operated similar to a rotor PM machine. To generate a torque, an air gap field with the same pole pair number as the rotor field $p_{\mathrm{drv}} = p_{\mathrm{rot}}$ has to be generated by the stator coils. Radial bearing forces are generated with a stator field that has a pole pair number of $p_{\mathrm{bng}} = p_{\mathrm{rot}} \pm 1$. Slice motors are implemented with concentrated windings, since ohmic losses in the winding head would be dominant for distributed windings. Both, combined and separated winding systems, can be used to generate an air gap field for torque and radial force generation. For the design presented in this work, separate drive and bearing coils are used.

TABLE 1. Parameters Used for Optimizing the Electromagnetic Design of the Machine Using FEM Simulations

	Variable	Unit	Description
	δ_{mag}	mm	air gap length (5 mm)
Rotor	r_{Ro}	mm	outer radius (50 mm)
	h_{R}	mm	height
	r_{Ri}, r_{Rm}	mm	inner and mid radius
	$w_{\mathrm{R,TH}}$, $\alpha_{\mathrm{R,TH}}$	mm, °	tooth width and angle
Stator	$w_{\mathrm{S,TH}}$, $h_{\mathrm{S,TH}}$	mm	tooth width and height
	$\delta_{\mathrm{S,TH}}$	mm	tooth depth
	$w_{\mathrm{S,L}}$, $\delta_{\mathrm{S,L}}$	mm	column width and depth
	h_{coil}	mm	coil height
	$h_{\mathrm{S,back}}$	mm	back iron height
	$w_{\mathrm{S,PM}}$	mm	PM width
	m_{PM}	kg	PM mass (5 kg)

C. ELECTROMAGNETIC DESIGN

All dimensions of the stator and the rotor, as listed in Table I, were optimized using magnetostatic FEM simulations in Ansys Maxwell [20]. Five rotor parameters and eight stator parameters were varied to obtain a suitable design. The optimizations were carried out to achieve the following objectives in decreasing order of importance:

1) Maximize average passive tilting stiffnesses over one revolution $\overline{k_{\alpha,\beta}}$
2) Maximize the motor torque T at nominal flux $\Theta_{\mathrm{drv,N}}$
3) Maximize passive axial stiffness k_{z}
4) Maximize the radial startup distance, i.e. the ratio of active radial force $F_{\mathrm{r,act,N}}$ at nominal flux $\Theta_{\mathrm{bng,N}}$ and the passive radial stiffness k_{r}
5) Minimize the cogging torque T_{cog}
6) Minimize the variation of the nominal torque ΔT_{N} over the rotor angle φ_{m}
7) Minimize the variation of the nominal bearing force $\Delta F_{\mathrm{r,act,N}}$ over φ_{m},

where a trade-off between these objectives exists (see below). This can be expressed mathematically as shown in (5), where w_1 to w_7 denote the relative weights assigned to the individual objective functions. The weights were chosen in accordance with the aforementioned priorities and based on experience from other bearingless motor designs [20], [29]. In order to eliminate the influence of the absolute values of the individual variables on their relative weight in the objective function, normalized versions, denoted by apostrophes, were used. For example,

$$\overline{k_{\alpha,\beta}}' = \frac{\overline{k_{\alpha,\beta}}}{\overline{k_{\alpha,\beta}}^{*}}, \tag{4}$$

where $\overline{k_{\alpha,\beta}}^{*}$ denotes the normalization value, in this case being equal to the optimal (maximum) value of $\overline{k_{\alpha,\beta}}$.

$$\max \begin{pmatrix} w_1 \\ w_2 \\ w_3 \\ w_4 \\ w_5 \\ w_6 \\ w_7 \end{pmatrix} \cdot \begin{pmatrix} \overline{k_{\alpha,\beta}}' \\ T'(\Theta_{\mathrm{drv,N}}) \\ k_z' \\ \min\left(F_{\mathrm{r,act,N}}'/k_{\mathrm{r}}'\right) \\ -T_{\mathrm{cog}}' \\ -\Delta T_{\mathrm{N}}' \\ -\Delta F_{\mathrm{r,act,N}}' \end{pmatrix} \tag{5}$$

Based on application requirements, the values for δ_{mag}, r_{Ro}, and m_{PM} were fixed to the values listed in parenthesis in Table 1 in order to impose boundary conditions that result in practically feasible motor designs. The ohmic motor losses at nominal flux were fixed to 200 W, which results in a maximum temperature inside the motor, particularly of the stator in the vicinity of the air gap, of $\approx 85\,^{\circ}\mathrm{C}$ for an ambient temperature of 40 °C. This value was chosen to achieve a sufficiently high MTBF of the components of the employed sensor electronics, which have to be placed close to the air gap. It was found that neither the windings nor the permanent magnets impose further thermal limitations under these conditions. As the highest thermal resistance (by far) is between the housing of the motor and the environment and internal temperature variations are relatively small for a potted machine, a detailed internal thermal analysis of the motor was not carried out. The exact thermal behavior was not considered during the optimization in order not to further increase the complexity. A total of approximately 80 designs were considered in this work. The simplex algorithm as implemented in Ansys Maxwell was used for the optimization analysis.

The nominal flux results from the coil geometry, where 2/3 and 1/3 of the available winding window were allocated to the drive and bearing coils, respectively. The low rotor height and large air gap result in significant stray flux above and below the rotor. Consequently, 3D simulations had to be carried out to obtain meaningful results. As this required significantly longer simulation times than for 2D simulations, the optimization procedure was carried out using two different simulation models:

1) In the first step, a flat motor model was used to optimize the geometry of the rotor and stator teeth close to the air gap without taking motor losses into account. The simulations were initialized using the minimum value for r_{Ri} and a small value for r_{Rm}. Based on this setup, the following parameters were optimized in the provided order:
   a) Horizontal geometry: $w_{\mathrm{S,TH}}$, $w_{\mathrm{R,TH}}$, and $\alpha_{\mathrm{R,TH}}$
   b) Vertical geometry: h_{R} and $h_{\mathrm{S,TH}}$
   c) Subsequently, r_{Ri} and r_{Rm} were increased as long as no performance degradation occurred.
2) In a second step, the results from 1) were transferred to the desired temple motor geometry. The simulations were initialized with the maximum value for $h_{\mathrm{S,back}}$. The radial depth of the back iron is chosen to be equal to $\delta_{\mathrm{S,L}}$. The following parameters were optimized in the provided order:
   a) Stator teeth: $\delta_{\mathrm{S,TH}}$, $w_{\mathrm{S,L}}$, $\delta_{\mathrm{S,L}}$
   b) Coils: h_{coil} (ohmic loss limit of 200 W)
   c) Subsequently, $h_{\mathrm{S,back}}$ was decreased as long as no performance degradation occurred.

The goal of the optimization step 2a) was to obtain the same performance for the temple geometry as for the flat geometry. The design is chosen such that the desired nominal flux is reached and has a value that fully utilizes the linear range (material characteristics) of the flat motor model without causing relevant (partial) saturation. This is particularly demanding, as the PMs are scaled with the stator geometry. Even without coil currents, flux densities close to the saturation limit are reached. As there is no convergence limit for the overall stator size and volume (larger geometry yields favorable properties), it was kept within feasible dimensions by limiting the mass of the PMs to a total of 5 kg, based on which the value of $w_{\mathrm{S,PM}}$ is determined.

The underlying design trade-offs are similar to those of bearingless slice motors in general. A detailed outline is provided, e.g., in [30]. Exemplarily, the trade-offs considered in step 1b) are described here: The achievable torque is maximized for $h_{\mathrm{R}} = h_{\mathrm{S,TH}}$ and high absolute values for both variables. This is in contradiction with the requirements for achieving high passive axial and tilting stiffnesses. For maximizing k_z, an optimal ratio of $h_{\mathrm{R}}/h_{\mathrm{S,TH}} \approx 0.9$ exists. No optimum absolute values for h_{R} and $h_{\mathrm{S,TH}}$ exist as k_z asymptotically approaches a maximum value for increasing h_{R} and $h_{\mathrm{S,TH}}$. Simultaneously, an optimal ratio of $h_{\mathrm{R}}/h_{\mathrm{S,TH}} \approx 0.7$ exists for maximizing $k_{\alpha,\beta}$. The provided numerical values are specific to the machine design and geometry at hand. In contrast to the axial stiffness, an additional optimum for the absolute values of h_{R} and $h_{\mathrm{S,TH}}$ exists for maximizing $k_{\alpha,\beta}$. This trade-off is addressed as follows: Starting from the values of h_{R} and $h_{\mathrm{S,TH}}$ that result in the maximum tilting stiffness, these values were altered such that T and k_z are increased while limiting the decrease of $k_{\alpha,\beta}$ to less than 20%.

D. FORCES AND TORQUES

Its capability to generate high tangential forces makes the considered FSPM topology well suited for achieving high toque densities [31]. At rotor angles for which a rotor and a stator tooth are aligned, the magnetic flux path is closed through the rotor, resulting an a high passive radial stiffness. However, due to the chosen stator topology and wiring scheme, it is not possible to generate radial bearing forces at this angle, as the flux generated by the PMs cannot be amplified or weakened on both sides of the rotor at the same time. Consequently, the high passive radial force can only be counteracted through neighboring teeth. This results in an unfavorable ratio of active and passive radial forces that makes the implementation of a magnetic bearing cumbersome, especially for a low number of rotor poles. The fluctuation of the radial forces over the

TABLE 2. Nominal Flux Values, Passive and Active Properties Averaged Over One Revolution of the Rotor

		FSPM PP6	FSPM PP9
$\Theta_{\mathrm{drv,N}}$	AT	1640	
$\Theta_{\mathrm{bng,N}}$	AT	1150	
$\overline{k_{\mathrm{r}}}$	N/mm	193	168
$\overline{k_{\mathrm{z}}}$	N/mm	14.1	15.6
$\overline{k_{\alpha,\beta}}$	Nm/°	0.37	0.44
$\overline{T}(\Theta_{\mathrm{drv,N}})$	Nm	8.10	6.30
$\overline{F_{\mathrm{r,act}}}(\Theta_{\mathrm{bng,N}})$	N	170	136

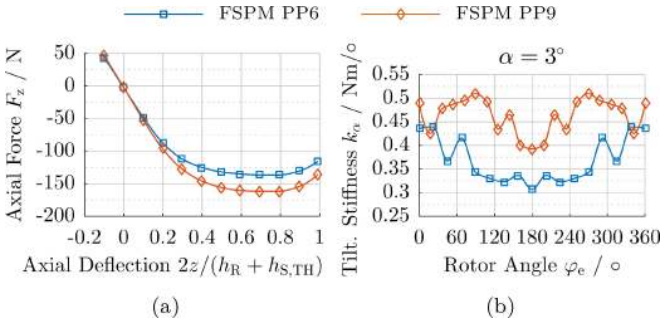

FIGURE 6. Passive axial restoring force versus normalized axial deflection (a) and tilting stiffness k_α versus rotor angle (b) of the implemented prototypes.

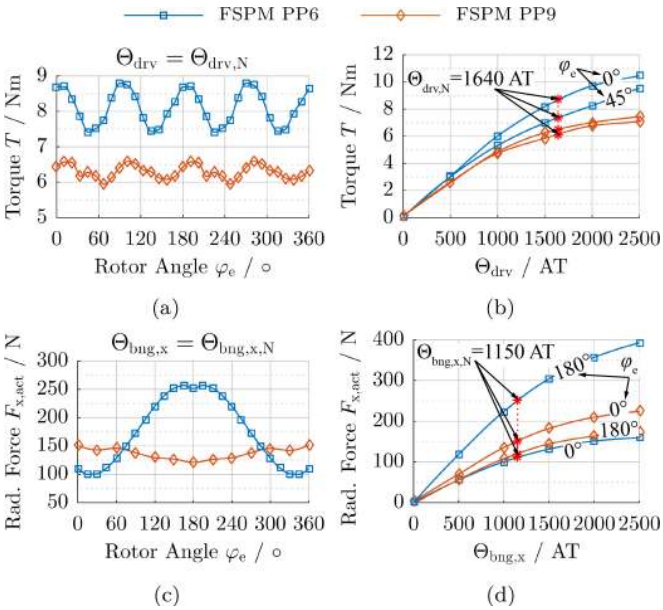

FIGURE 7. Motor torque versus rotor angle at nominal drive flux $\Theta_{\mathbf{drv,N}}$ (a), torque for different values of $\Theta_{\mathbf{drv}}$ (b), active radial force versus rotor angle at nominal bearing flux $\Theta_{\mathbf{bng,N}}$ (c), and active radial force for different values of $\Theta_{\mathbf{bng}}$ (d) of the implemented prototypes. The characteristics shown in (b) and (d) have been obtained for the two rotor angles at which their extreme values are reached.

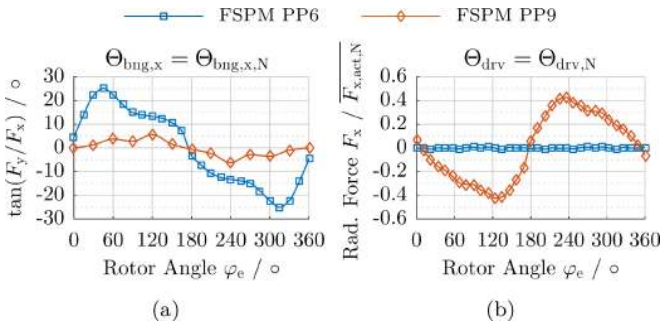

FIGURE 8. Deviation angle between desired and actual radial bearing force (a), and parasitic radial force caused by the nominal drive flux normalized to the nominal active radial force.

rotor angle can be reduced by using a rotor with an odd pole pair number, such as the presented FSPM PP9. However, a drive current results in strong parasitic radial forces in such a topology, as analyzed below. Moreover, the geometries of the stator and rotor teeth have to be well matched in order to prevent radial forces when turning the rotor, even without any coil currents.

Table 2 lists the nominal flux values for the drive $\Theta_{\mathrm{drv,N}}$ and bearing $\Theta_{\mathrm{bng,N}}$ that are reached for the obtained design for ohmic losses of 200 W each. Moreover, a summary of the passive and active forces and torques that are reached at the nominal flux is provided. The values were obtained by averaging over one revolution of the rotor. The values for $\overline{k_{\alpha,\beta}}$, $\overline{k_{\mathrm{r}}}$, and $\overline{k_{\mathrm{z}}}$ were obtained for a tilting angle of $\alpha = 3°$, a radial displacement of 2 mm, and an axial displacement of ±6 mm, respectively.

The passive axial restoring force versus the normalized axial displacement of the rotor and the tilting stiffness versus the electrical rotor angle are shown in Figs. 6(a) and (b), respectively. The axial restoring force is mostly independent of the rotor angle. The cogging torque of both topologies is at a negligible level due to the conducted geometrical optimizations. Figures 7(a) and (c) show the torque and active radial force in the x-direction for the nominal flux values, respectively. Figures 7(b) and (d), show the same characteristics for different values of $\Theta_{\mathrm{drv,N}}$ and $\Theta_{\mathrm{bng,N}}$. The rotor angles at which their minimum and maximum values occur are noted next to the respective curves. The nominal flux values are marked by red asterisks, which shows that a similar operating region at the onset of saturation is obtained for both topologies.

Based on these characteristics, the controllability of the motor can be analyzed. One relevant metric is the deviation between the desired and the actual angle of the radial bearing force, which is displayed in Fig. 8(a). It can be seen that the FSPM PP6 topology exhibits deviations of up to 25°, which complicates the control and has to be compensated in software (see Section IV). Contrarily, no large angle deviations exist for the PP9 with an uneven pole pair number. However, as discussed above, this topology exhibits an undesired parasitic radial force of up to 45% of its nominal value if a drive current is applied. This is illustrated in Fig. 8(b).

TABLE 3. Controllability Comparison for the PP6 and PP9 Rotors: (a) Fluctuation of the Drive Torque, (b) Normalized Cogging Torque, (c) Fluctuation of the Active Radial Force, (d) Angular Deviation of the Active Radial Force, (e) Normalized Parasitic Radial Force Due to a Drive Current, (f) Minimum and (g) Maximum Startup Distance, (h) Fluctuation of the Tilting Stiffness

	FSPM PP6	FSPM PP9
(a) ΔT_N	$\pm 8.5\,\%$	$\pm 5.2\,\%$
(b) T_cog / $\overline{T_\mathrm{N}}$	$\pm 2.4\,\%$	$\pm 1.8\,\%$
(c) $\Delta F_{\mathrm{r,act,N}}$	$\pm 44\,\%$	$\pm 11\,\%$
(d) $\angle F_{\mathrm{r,act,N}}$	$\pm 25°$	$\pm 5.6°$
(e) $F_\mathrm{r}(\Theta_\mathrm{drv,N})/\overline{F_{\mathrm{r,act,N}}}$	$\pm 0.8\,\%$	$\pm 43\,\%$
(f) $\min(F_{\mathrm{r,act,N}}/k_\mathrm{r})$	0.66 mm	0.64 mm
(g) $\max(F_{\mathrm{r,act,N}}/k_\mathrm{r})$	1.12 mm	1.02 mm
(h) $\Delta k_{\alpha,\beta}$	$\pm 22\,\%$	$\pm 27\,\%$

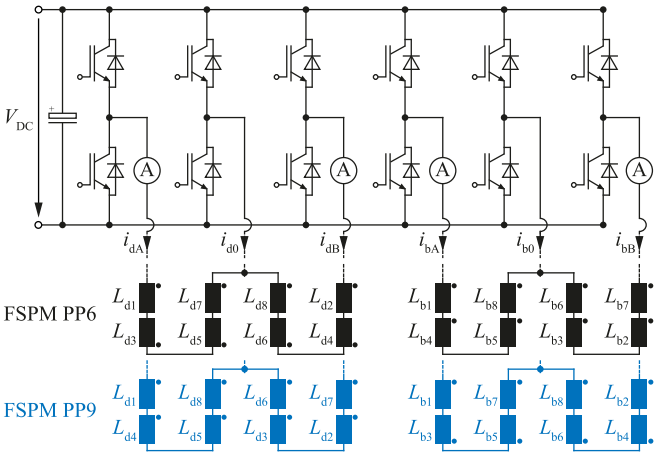

FIGURE 9. Connection scheme of the drive (index d) and bearing (index b) coils, each featuring two phases, to a six-phase bearingless motor controller. The connection scheme is shown in black and blue for the FSPM PP6 and FSPM PP9, respectively.

The possible radial startup distance is a further metric for assessing the controllability. Due to the low active forces and high passive radial stiffness, this distance is significantly smaller for FSPM topologies than for other bearingless motors [10]. The high passive stiffness also requires a high bandwidth controller in order to obtain stable levitation of the rotor.

A quantitative summary of the discussed results is provided in Table 3, where critical characteristics are marked in red.

E. POWER ELECTRONICS

Using separate drive and bearing windings results in a design with two drive phases consisting of four coils each and two bearing phases consisting of four coils each. The total of sixteen motor coils are connected to a power electronic converter with six IGBT half-bridges and four current sensors as shown in Fig. 9. The numbering of the coils coincides with that provided in Fig. 1. In the case of combined windings, a converter with eight phases and additional current sensors would be required. Two half bridges with current sensors are

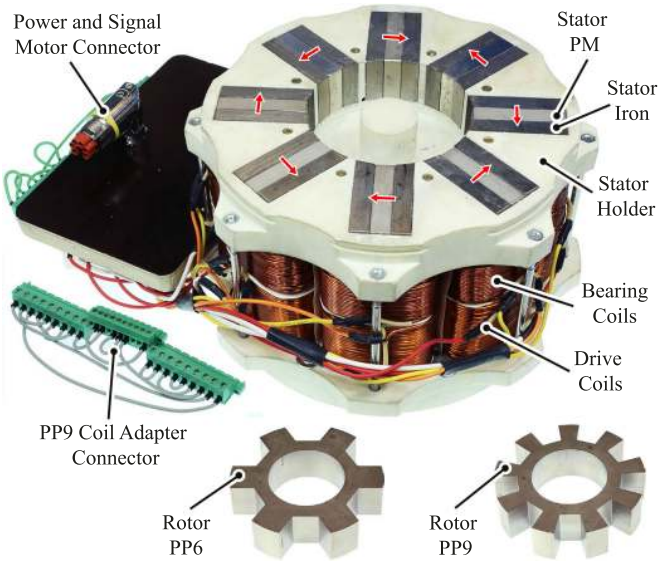

FIGURE 10. Assembled prototypes: Stator with coil adapter connector as well as PP6 and PP9 rotors.

connected to the phases A and B of the drive and bearing each. The third half bridge is used as the return path for both phases and is operated at 50% duty-cycle. The DC-link voltage of $\approx$320 V is generated by a diode bridge rectifier. The connection scheme is different for the FSPM PP6 and FSPM PP9, as shown in black and blue in Fig. 9, respectively. Alternation between the two connection schemes is implemented by a coil adapter connector, as shown in Fig. 10.

IV. EXPERIMENTAL RESULTS

Prototypes of the stator and the two rotors PP6 and PP9, that were optimized according to the procedure outlined in the previous section, were implemented and are shown in Fig. 10. A 3D-printed support structure at the upper and lower ends of the stator is used to increase its mechanical stability. The stator contains the chosen maximum value of 5 kg of N45 grade NdFeB PM material.

A. CONTROL

The four remaining degrees of freedom resulting from the connection scheme of the motor coils to the power electronic converter are used to control the radial position of the rotor in the x and y direction, as well as the rotational speed ω_m through controlling the direct and quadrature component of the drive current $i_\mathrm{drv,d}$ and $i_\mathrm{drv,q}$, respectively. The outer loops of cascaded controllers generate reference values for a virtual drive current $i_\mathrm{drv,q}$ and virtual bearing currents $i_\mathrm{bng,x}$, $i_\mathrm{bng,y}$ that are directly proportional to the torque T and radial forces F_x, F_y, respectively. A magnetization current is not required, resulting in $i_\mathrm{drv,d} = 0$. In order to transform the aforementioned virtual current components into the actual phase currents, they have to be rotated by the rotor angle. For

TABLE 4. Bearing and Drive Inductances for the FSPM PP6 and PP9 Prototype With the Rotor in Place

		FSPM PP6	FSPM PP9
L_{drv}	mH	26.1	34.3
L_{bng}	mH	25.9	21.8

the considered motor design with eight stator teeth and separated windings, additional transformations, such as required for combined windings, are not necessary due to the wiring of the coils. For the PP6 rotor ($p_{\mathrm{rot}} = 6$) a stator field with $p_{\mathrm{drv}} = 6$ and $p_{\mathrm{bng}} = 7$ is generated. Similarly, for the PP9 rotor ($p_{\mathrm{rot}} = 9$) a stator field with $p_{\mathrm{drv}} = 9$ and $p_{\mathrm{bng}} = 10$ is generated (see Section III-B).

In order to obtain stable magnetic levitation of the rotor, despite the challenges discussed in Section III-D, further adaptions to the control scheme had to be made. The large fluctuations of the active radial force result in a small radial startup distance of 0.65 mm for the angle at which the force is minimal (cf. Table 3). While this is just 13% of δ_{mag}, the startup distance is commonly limited to a sufficiently low value by the wall of a process chamber, such as shown in Fig. 15. Nevertheless, a short-time bearing current of 150% of its nominal value is required during radial startup. The high passive radial stiffness results in a high eigenfrequency of rotor oscillations in the radial direction. As a result, the bandwidth requirements for the bearing controller are significantly higher than for state-of-the-art rotor PM bearingless motors. The existing lowpass filters in the sensor systems, the firmware (digital filters), and the power electronic converter were adjusted to a higher cutoff frequency, which resulted in increased audible noise. The bearing coils had to be implemented with a low number of turns to achieve a sufficiently low inductance and high dynamics. Values for the resulting drive and bearing inductances with the rotor in place are provided in Table 4.

To compensate for the angle-dependent fluctuation of the radial bearing force of $\pm$ 44% and angle deviation of $\pm$ 25° for the FSPM PP6, as shown in Fig. 8 and Table 3, the position controller was modified as shown in Fig. 11(a). Here, T denotes the Park transformation. The angle-dependent fluctuation of the radial bearing force is accounted for by multiplying the reference forces by a correction factor k_{corr}. This factor is obtained from the lookup table kLUT based on the angle φ_{e} as an input. To account for the angle deviation of the force, the input angle to the Park transformation is calculated as $\varphi_{\mathrm{e}} + \alpha_{\mathrm{corr}}$, where the correction angle is obtained from the lookup table αLUT that requires φ_{e} and the reference bearing current as inputs. This feed-forward correction further increases the control bandwidth requirements, as harmonic current components of the fundamental rotational frequency need to be impressed in the coils. This limited the achievable rotational speed at which stable levitation of the rotor was attainable to $\approx$2000 rpm.

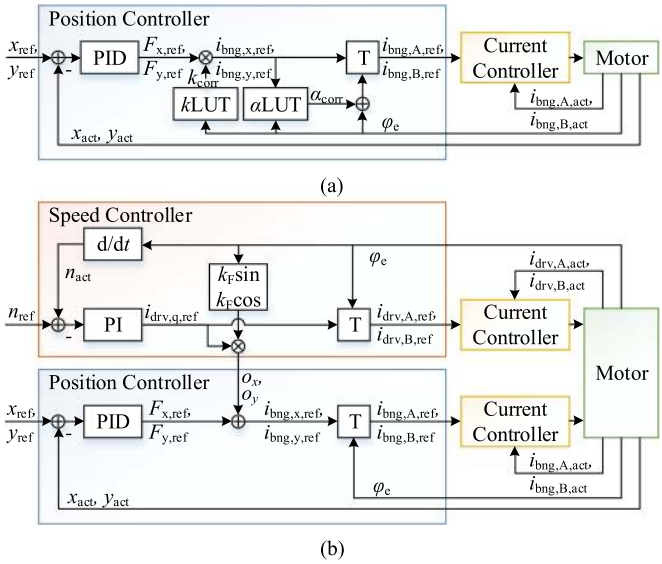

FIGURE 11. Control scheme adaptions: Compensation of the rotor-angle-dependent amplitude fluctuation and force angle deviation for the PP6 rotor (a), and compensation of the parasitic radial force caused by torque generation for the PP9 rotor (b).

For the FSPM PP9, stable levitation and rotation at low torque is possible without further modifications to the controller. For higher torques, the parasitic radial force of up to $\pm$43% of the nominal active radial force requires adjustments to the position controller, where additional inputs are required from the speed controller, as depicted in Fig. 11(b). The parasitic radial force characteristic, as shown in Fig. 8(b), is approximated by a sinusoidal function. Based on the reference value of the q-current, the offsets $o_{\mathrm{x}} = k_{\mathrm{F}} \sin(\varphi_{\mathrm{e}}) i_{\mathrm{drv,q,ref}}$ and $o_{\mathrm{y}} = k_{\mathrm{F}} \cos(\varphi_{\mathrm{e}}) i_{\mathrm{drv,q,ref}}$ are calculated, where k_{F} is determined by the magnitude of the parasitic force. These offsets are added to the reference values of the bearing forces in the position controller, in order to obtain the corrected reference bearing currents.

B. TORQUE VERIFICATION

The motor torque at standstill was measured using two spring balances that were fixed to the levitating rotor. The shaded areas shown in Fig. 12 indicate the expected torque range between the angle resulting in the minimum and maximum torque. It can be seen that these two mechanical angles are close to each other (within 5° for the PP9 rotor), making it difficult to obtain exact alignment during experiments. The measurements were conducted for different values of the magnetic flux Θ_{drv}. It can be seen that the measured values for the torque coincide well with the simulation results and that the onset of saturation is correctly projected. At nominal drive flux, the FSPM PP6 and FSPM PP9 reaches a torque of 8 Nm and slightly above 6 Nm, respectively.

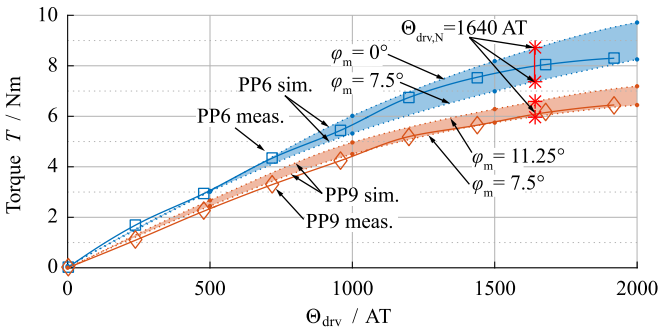

FIGURE 12. Simulated and measured torque at standstill for different values of the drive flux Θ_{drv}.

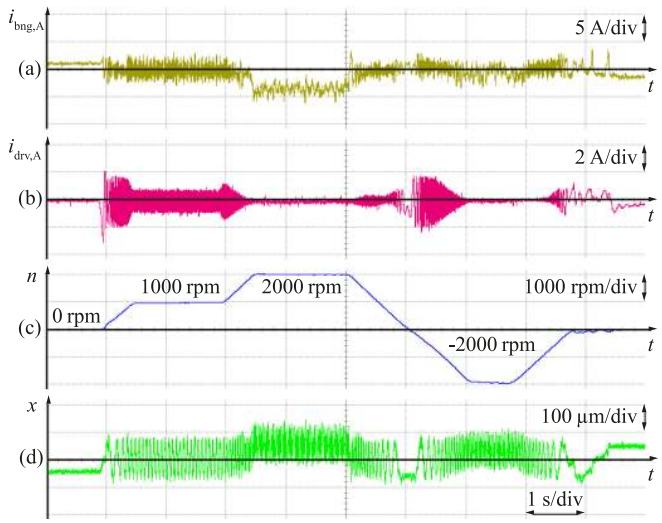

FIGURE 13. Measured data for an exemplary 10 s cycle of rotational speeds between plus and minus 2000 rpm with the FSPM PP6 prototype running in air and without additional load: bearing current (a), drive current (b), rotational speed (c), and radial position (d).

C. DYNAMIC BEHAVIOUR

Maximum rotational speeds of 2000 rpm and 2300 rpm were reached in air and without additional load for the PP6 and PP9 rotors, respectively. Higher rotational speeds could not be achieved due to unstable levitation of the rotor, despite the back-EMF limit of the prototype being ≈4000 rpm. For the FSPM PP6, Fig. 13 shows the bearing and drive currents, as well as the rotational speed and radial position for a ten second cycle consisting of an acceleration from standstill to 1000 rpm and further to 2000 rpm, followed by a reversal of the rotational direction to −2000 rpm and, finally, deceleration back to standstill. The visible first order harmonics of the position signal x are caused by a small eccentricity of the rotor. This effect is attenuated by the bearing controller as reflected in $i_{bng,A}$. It can be seen that the drive current $i_{drv,A}$ remains below 4 A peak-to-peak for all conditions of the test cycle.

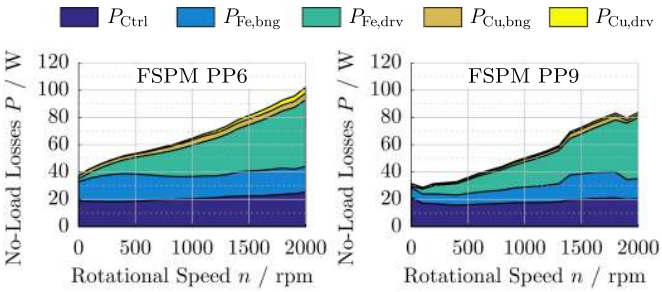

FIGURE 14. No-load loss components at different rotational speeds for the FSPM PP6 and FSPM PP9.

D. LOSSES

The presented prototype was optimized for applications that require high torque at low rotational speeds where iron losses can be neglected. Nevertheless, the no-load motor losses, including their individual components, were measured up to the maximum achievable rotational speed. The results are shown in Fig. 14, where P_{Ctrl} denote the losses caused by the power electronic circuit used to control the motor. $P_{Fe,bng}$ and $P_{Cu,bng}$ denote the iron and copper (ohmic) losses due to magnetic bearing force generation. Similarly, $P_{Fe,drv}$ and $P_{Cu,drv}$ denote the iron and copper losses due to torque generation.

The power delivered to the separate bearing and drive windings (cf. Fig. 9), corresponding to the overall no-load losses due to the bearing and drive, respectively, were measured separately (at the same time) using a high precision power analyzer (Yokogawa WT1804E). Additionally, the respective currents were measured using the same device. Based on the measured currents and the phase resistances, the values for $P_{Cu,bng}$ and $P_{Cu,drv}$ were calculated. Subsequently, the values for $P_{Fe,bng}$ and $P_{Fe,drv}$ were obtained by subtracting the respective copper losses from the measured overall losses obtained in the first step.

It can be observed that the copper losses are at negligible levels, as expected for no-load operation. At nominal torque, $P_{Cu,drv}$ increases to 200 W as designed. At high rotational speeds $P_{Fe,drv}$ becomes the dominant loss component. A possible approach for reducing these losses in future applications that require higher rotational speeds would be to use soft magnetic composite material [32] for the three-dimensional flux path of the temple configuration.

E. APPLICATION SCENARIO

The presented prototype was operated in a mixing application with a tank volume of 1000 L. The used tank flange is shown in Fig. 15. The figure also shows a rendering of the designed mixing blade including a clamp-on mechanism to connect it to the rotor as well as a photograph of its implementation. A superior tilting stability of the rotor in water, compared to a state-of-the-art bearingless motor with a single-pole-pair PM rotor, was observed. The reason for this is that the tilting stiffness of the presented machine topology is relatively

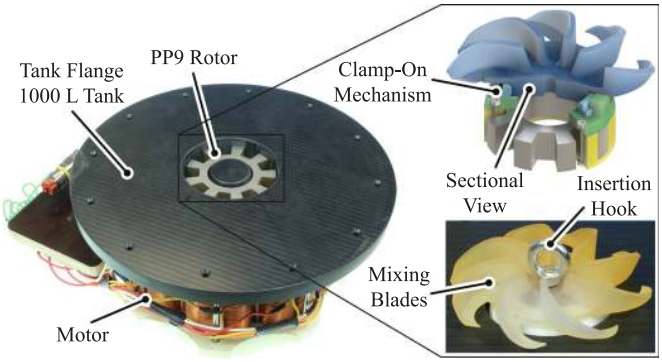

FIGURE 15. **FSPM PP9 with mounted tank flange, as well as mixing blade and clamp-on mechanism. The shown insertion hook was used to insert and remove the rotor from the filled 1000 L tank.**

constant over an entire revolution due to the higher number of pole-pairs. Therefore, an already tilted rotor, e.g., due to hydraulic loading of the mixing blade, does not excite further vibrations or even resonances.

V. CONCLUSION

The topology, design procedure, and prototype implementation of a new bearingless slice motor topology that provides both higher rotor torque density and a larger ratio of the air gap to rotor radius, compared to previously published topologies, has been presented. It is well suited for applications where a steel rotor is beneficial, such as for high circumferential speeds, high ambient temperatures, or rotor disposable applications. By adapting the control scheme to compensate for parasitic bearing force components as presented, stable operation up to 2000 rpm and a torque of 8 Nm were reached. Regarding the selection of an odd or even pole pair number, a trade-off between controllability and torque exists. On the one hand, the rotor with an even pole pair number (PP6) provides high torque, while its control to achieve stable levitation is challenging. On the other hand, the rotor with an odd pole pair number (PP9) results in a lower torque, but the required bandwidth of the bearing controller is lower, providing improved levitation stability. Nevertheless, as stable suspension of the rotor could be obtained for both designs, it is anticipated that stable levitation can also be attained for a design with six stator teeth and seven (PP7, odd) or even only four (PP4, even) rotor teeth. Such designs would facilitate even larger air gaps and will be explored in the future.

REFERENCES

[1] A. Chiba, T. Fukao, O. Ichikawa, M. Oshima, M. Takemoto, and D. G. Dorrell, *Magnetic Bearings and Bearingless Drives*. Amsterdam, The Netherlands: Elsevier, 2005.

[2] F. De Robertis, E. Birks, P. Rogers, G. Dreyfus, J. Pepper, and A. Khaghani, "Clinical performance with the levitronix centrimag short-term ventricular assist device," *J. Heart Lung Transplantation*, vol. 25, no. 2, pp. 181–186, 2006.

[3] P. Peralta, T. Wellerdieck, D. Steinert, T. Nussbaumer, and J. W. Kolar, "Ultra-high temperature bearingless permanent magnet pump for aggressive fluids," *IEEE/ASME Trans. Mechatronics*, vol. 22, no. 5, pp. 2392–2394, Oct. 2017.

[4] T. Shinshi, R. Yamamoto, Y. Nagira, and J. Asama, "A bearingless slice motor with a solid iron rotor for disposable centrifugal blood pump," in *Proc. Int. Power Electron. Conf. (IPEC-Niigata Asia)*, May 2018, pp. 4016–4019.

[5] C. Schirmer, T. Nussbaumer, R. Schöb, R. Pörtner, R. Eibl, and D. Eibl, "Development, engineering and biological characterization of stirred tank bioreactors," in *Biopharmaceuticals*. London, U.K.: IntechOpen, 2018.

[6] R. Schoeb and N. Barletta, "Principle and application of a bearingless slice motor," *JSME Int. J. Ser. C Mech. Syst., Mach. Elements Manuf.*, vol. 40, no. 4, pp. 593–598, 1997.

[7] W. Gruber, W. Briewasser, M. Rothböck, and R. T. Schöb, "Bearingless slice motor concepts without permanent magnets in the rotor," in *Proc. IEEE Int. Conf. Ind. Technol.*, Feb. 2013, pp. 259–265.

[8] W. Gruber, W. Briewasser, and W. Amrhein, "Novel bearingless slice motor design with four concentrated coils featuring a unique operational behavior," in *Proc. 14th Eur. Conf. Power Electron. Appl.*, Aug. 2011, pp. 1–10.

[9] W. Gruber, M. Rothböck, and R. T. Schöb, "Design of a novel homopolar bearingless slice motor with reluctance rotor," *IEEE Trans. Industry Appl.*, vol. 51, no. 2, pp. 1456–1464, Mar. 2015.

[10] W. Gruber, K. Radman, and R. T. Schöb, "Design of a bearingless flux-switching slice motor," in *Proc. Int. Power Electron. Conf. (IPEC-Hiroshima Asia)*, May 2014, pp. 1691–1696.

[11] Q. Li, P. Boesch, M. Haefliger, J. W. Kolar, and D. Xu, "Basic characteristics of a 4kW permanent-magnet type bearingless slice motor for centrifugal pump system," in *Proc. Int. Conf. Elect. Mach. Syst.*, Oct. 2008, pp. 3037–3042.

[12] P. Karutz, T. Nussbaumer, W. Gruber, and J. W. Kolar, "Novel magnetically levitated two-level motor," *IEEE/ASME Trans. Mechatronics*, vol. 13, no. 6, pp. 658–668, Dec. 2008.

[13] F. Zurcher, T. Nussbaumer, W. Gruber, and J. W. Kolar, "Design and development of a 26-pole and 24-Slot bearingless motor," *IEEE Trans. Magn.*, vol. 45, no. 10, pp. 4594–4597, Oct. 2009.

[14] B. Warberger, R. Kaelin, T. Nussbaumer, and J. W. Kolar, "50- /2500-W bearingless motor for high-purity pharmaceutical mixing," *IEEE Trans. Ind. Electron.*, vol. 59, no. 5, pp. 2236–2247, May 2012.

[15] N. Barletta and R. Schoeb, "Design of a bearingless blood pump," in *Proc. 3rd Int. Symp. Magn. Suspension Technol.*, 1996, pp. 265–274.

[16] M. Noh, W. Gruber, and D. L. Trumper, "Hysteresis bearingless slice motors with homopolar flux-biasing," *IEEE/ASME Trans. Mechatronics*, vol. 22, no. 5, pp. 2308–2318, Oct. 2017.

[17] W. Hua, M. Cheng, Z. Q. Zhu, and D. Howe, "Analysis and optimization of back EMF waveform of a flux-switching permanent magnet motor," *IEEE Trans. Energy Convers.*, vol. 23, no. 3, pp. 727–733, Sep. 2008.

[18] J. T. Chen and Z. Q. Zhu, "Comparison of all- and alternate-poles-wound flux-switching pm machines having different stator and rotor pole numbers," *IEEE Trans. Industry Appl.*, vol. 46, no. 4, pp. 1406–1415, Jul. 2010.

[19] N. Turk, N. Bulić, and W. Gruber, "Nonlinear control of a bearingless flux-switching slice motor with combined winding system," *IEEE/ASME Trans. Mechatronics*, vol. 25, no. 1, pp. 152–163, Feb. 2020.

[20] T. Holenstein, J. Greiner, D. Steinert, and J. W. Kolar, "A high torque, wide air gap bearingless motor with permanent magnet free rotor," in *Proc. IEEE Int. Electric Mach. Drives Conf.*, May 2017, pp. 1–6.

[21] S. Silber, W. Amrhein, P. Bosch, R. Schob, and N. Barletta, "Design aspects of bearingless slice motors," *IEEE/ASME Trans. Mechatronics*, vol. 10, no. 6, pp. 611–617, Dec. 2005.

[22] T. Reichert, T. Nussbaumer, W. Gruber, and J. W. Kolar, "Bearingless permanent-magnet motor with 4/12 Slot-pole ratio for bioreactor stirring applications," *IEEE/ASME Trans. Mechatronics*, vol. 16, no. 3, pp. 431–439, Jun. 2011.

[23] F. Zürcher, T. Nussbaumer, and J. W. Kolar, "Motor torque and magnetic levitation force generation in bearingless brushless multipole motors," *IEEE/ASME Trans. Mechatronics*, vol. 17, no. 6, pp. 1088–1097, Dec. 2012.

[24] D. Steinert, T. Nussbaumer, and J. W. Kolar, "Evaluation of one- and two-pole-pair slotless bearingless motors with toroidal windings," *IEEE Trans. Industry Appl.*, vol. 52, no. 1, pp. 172–180, Jan. 2016.

[25] P. Püntener, M. Schuck, D. Steinert, T. Nussbaumer, and J. W. Kolar, "A 150000 rpm bearingless slice motor," *IEEE/ASME Trans. Mechatronics*, vol. 23, no. 6, pp. 2963–2967, Dec. 2018.

[26] H. Bleuler *et al.*, *Magnetic Bearings: Theory, Design, and Application to Rotating Machinery*. Berlin, Germany: Springer, 2009.
[27] T. Stallinger, E. Göbl, R. Remplbauer, and W. Gruber, "Performance evaluation of a novel bearingless PM Vernier motor," in *Proc. IEEE 12th Int. Conf. Power Electron. Drive Syst.*, Dec. 2017, pp. 408–413.
[28] W. Gruber, R. Remplbauer, and E. Göbl, "Design of a novel bearingless permanent magnet Vernier slice motor with external rotor," in *Proc. IEEE Int. Electric Mach. Drives Conf.*, May 2017, pp. 1–6.
[29] T. Holenstein, T. Nussbaumer, and J. W. Kolar, "A bearingless synchronous reluctance slice motor with rotor flux barriers," in *Proc. IEEE Int. Power Electron. Conf. (IPEC-Niigata Asia)*, 2018, pp. 3619–3626.
[30] M. Schuck, P. Puentener, T. Holenstein, and J. W. Kolar, "Scaling and design of miniature high-speed bearingless slice motors," *e & i Elektrotechnik Informationstechnik*, vol. 136, no. 2, pp. 112–119, 2019.
[31] Z. Q. Zhu and J. T. Chen, "Advanced flux-switching permanent magnet brushless machines," *IEEE Trans. Magn.*, vol. 46, no. 6, pp. 1447–1453, Jun. 2010.
[32] J. Asama, T. Oiwa, T. Shinshi, and A. Chiba, "Experimental evaluation for core loss reduction of a consequent-pole bearingless disk motor using soft magnetic composites," *IEEE Trans. Energy Convers.*, vol. 33, no. 1, pp. 324–332, Mar. 2018.

THOMAS HOLENSTEIN (Student Member, IEEE) was born in 1984 in St. Gallen, Switzerland. He received the M.Sc degree in electrical engineering and information technology from the ETH Zurich, Switzerland, in 2009. During his studies, he focused on power electronics and mechatronics. In his master thesis, he developed new control algorithms for magnetically levitated motors. Since 2010 he is working as an R&D Engineer with the company Levitronix. Since 2015 he is a Ph.D. Student at the Power Electronic Systems Laboratory, ETH Zurich, where he is working on new motor concepts for magnetically levitated single-use drives.

MARCEL SCHUCK (Member, IEEE) received the B.Sc. degree in electrical and computer engineering from the Technische Universität Darmstadt, Germany, in 2011 and the M.Sc. degree in the same field from the University of Illinois at Urbana-Champaign in 2013. He received an MBA degree from the Collège des Ingénieurs in Paris, France in 2014. He was a Ph.D. Student at the Power Electronic Systems Laboratory at ETH Zurich, Switzerland from 2014 to 2017, where he is currently working as a Postdoctoral Researcher. His research interests include ultra-high speed bearingless machines, acoustic levitation, and mechatronic systems.

JOHANN W. KOLAR (Fellow, IEEE) received the M.Sc. and Ph.D. degrees (summa cum laude) from the Vienna University of Technology, Vienna, Austria. He is currently a Full Professor with and the Head of the Power Electronic Systems Laboratory, Swiss Federal Institute of Technology Zurich (ETH Zurich), Zurich, Switzerland. He has proposed numerous novel pulsewidth-modulation converter topologies and modulation and control concepts, published more than 650 scientific papers in international journals and conference proceedings, and filed more than 110 patents. The focus of his current research is on ultracompact and ultraefficient converter topologies employing latest power semiconductor technology (SiC and GaN), wireless power transfer, solid-state transformers, power supplies on chip, and ultra-high speed and bearingless motors. Prof. Kolar was a recipient of 21 IEEE Transactions and conference prize paper awards, the 2014 SEMIKRON Innovation Award, the 2014 IEEE Power Electronics Society R. David Middlebrook Award, and the ETH Zurich Golden Owl Award for Excellence in teaching.